Intrinsically Stretchable, Semi-transparent Organic Photovoltaics with High Efficiency and Mechanical Robustness via Full Solution Process

Jiaming Huang[1], Zhen Lu[1], Jiaqi He[1,2], Hong Hu[3], Qiong Liang[1], Kuan Liu[1], Zhiwei Ren[1], Yaokang Zhang[2], Hongyu Yu[2], Zijian Zheng[3] and Gang Li[1]*

J. Huang, Z. Lu, J. He, Q. Liang, Dr. K. Liu, Dr. Z. Ren, and Prof. G. Li

Department of Electronic and Information Engineering, Research Institute for Smart Energy (RISE), The Hong Kong Polytechnic University, Hung Hom, Kowloon, Hong Kong, China.

The Hong Kong Polytechnic University Shenzhen Research Institute, Shenzhen 518057, China.

E-mail: gang.w.li@polyu.edu.hk

J. He, Prof. H. Yu

School of Microelectronics, Southern University of Science and Technology, Shenzhen, China

Dr. H. Hu, Dr. Y. Zhang, Prof. Z. Zheng

Laboratory for Advanced Interfacial Materials and Devices, Institute of Textiles and Clothing, The Hong Kong Polytechnic University, Hung Hom, Kowloon, Hong Kong, China.

Keywords: Organic photovoltaic; Full solution process; Semi-transparent; Intrinsically stretchable; silver nanowires

Abstract

Intrinsically stretchable organic photovoltaic (*is*-OPV) with high efficiency and transparency remains a grand challenge for wearable applications. Herein, we report a full-solution processed device framework for semi-transparent *is*-OPV. A ferroconcrete-liked AZO@silver nanowires (AgNWs)@AZO (AAA) composite forms the back stretchable transparent electrode (STE), which not only offers a 3D long-range pathway for efficient charge transport and collection but also reinforces interfacial stability. The OPV based on AAA exhibits a power conversion efficiency (PCE) of 12.83% with an average visible transmittance of 26.7%. Furtherly, by employing thermoplastic polyurethane embedded AgNWs as the front STE, the semi-transparent *is*-OPV based on the full solution process achieved a record PCE of 10.90%. The *is*-OPV also exhibited excellent mechanical robustness, which remains 76.5% of initial PCE after 500 cycles of 10% stretch-release. This work sets a foundation for constructing a semi-transparent *is*-OPV from a full solution process for wearable applications and skin-like electronics.

Introduction

Wearable power suppliers bring huge potential in self-powered sensing, health monitoring, human-computer interactions (HCIs), and the Internet of Things (IoT).[1-4] Stretchability and transparency are needed for power suppliers to satisfy the reliability and aesthetics of wearable applications.[5-9] Among various emerging power suppliers, organic photovoltaic (OPV) has been regarded as one of the most promising candidates due to the unique features of non-toxic, high power-per-weight output, semi-transparency, and intrinsic stretchability of the photoactive materials.[10-13] Currently, the power conversion efficiency (PCE) of OPV based on rigid configurations has surpassed 19% for the single-junction device.[14-18] To fully unleash the potential of OPV in wearable applications, the explosion of stretchable and semi-transparent configurations is essential.

Structural engineering including pre-strains and buckling has been usually employed to construct stretchable OPVs from rigid or flexible components.[19-23] But these approaches are sophisticated and the obtained devices suffer limited stretchability and uneven deformation. In contrast, intrinsically stretchable OPV (*is*-OPV) at the material level is ideal for achieving high stretchability and easy processing and is potentially compatible with Sheets-on-Shuttle manufacturing.[24] Successful *is*-OPV requires that all the layers should be stretchable, mechanically stable, and in contact tightly with each other. However, traditional high-performed materials, especially the electrode such as indium tin oxide (ITO) and metals (*e. g.* Ag, Au) cannot satisfy *is*-OPV requirements due to their brittleness. Depositing these electrodes based on vacuum-assisted systems (*e. g.* thermal evaporation, e-beam, and sputtering) is expensive, time-consuming, incompatible with flexible substrates, and limited by the finite chamber, which impedes large-area productions. Printable liquid metal such as eutectic gallium indium (eGaIn) is another typical stretchable back electrode candidate for *is*-OPV but does not support high transparency.[25-29] Moreover, the low viscosity and high surface tension of liquid metal leads to an unfixed shape and poor wettability and adhesion to the underlying substrate, which impedes the practicality of the OPV. In this case, achieving semi-transparent *is*-OPV is still challenging.

Printable silver nanowires (AgNWs) are a promising candidate for the electrode in semi-transparent *is*-OPV due to their excellent conductivity, transparency, and stretchability.[30-35] However, obtaining high-performed solution-processed AgNWs back electrodes in OPV is difficult due to the following issues. On the one hand, the post-treatments like high-temperature annealing, plasmonic, chemical welding, and mechanical press are needed to achieve high-conductive AgNWs networks.[36-39] These harsh post-treatments are not suitable for the back electrode due to the negative effect on underlying functional layers. Transfer printing is a possible method but requires complicated procedures.[40-42] On the other hand, unlike the high-quality contact of transport layer/metal from thermal deposition, directly coating AgNWs on transport layers would suffer from serious electric/mechanical contact issues which greatly influence the mechanical stability and the photovoltaic performance.[43-45]

Recent advanced OPV devices based on AgNWs back electrode almost show poor FF of <70%, which is much lower than the counterpart of the thermally evaporated metal electrode. Therefore, reliable back electrodes for *is*-OPV are needed.

In this work, we present the first report of high-efficient semi-transparent *is*-OPVs from a full solution process. All the functional layers (including substrate and electrode) are prepared by the solution process and exhibit both semi-transparency and good stretchability. First, a novel reinforced concrete-liked structure of Al-doped zinc oxide (AZO)@silver nanowires (AgNWs)@AZO (AAA) is achieved as the back stretchable transparent electrode (STE) for semi-transparent *is*-OPV. Importantly, the theoretically simulated and experimental results show that the AAA exhibits a 3D bundling structure that provides a long-range pathway for efficient charge transport and collections as well as robust mechanical stability. The semi-transparent rigid device based on a solution-processed AAA back electrode shows a 12.83% PCE with an average transmittance (AVT) of 26.7%, which is comparable to the device based on vacuum-evaporated ultra-thin Ag. Moreover, the 3D bundling structure of the AAA enables outstanding stretchability as well as strong adhesion. Furthermore, by cooperating with the AgNWs embedded thermoplastic polyurethane (TPU@AgNWs) front STE and AAA back STE, we demonstrated the record PCE of 10.90 % for semi-transparent *is*-OPV. More promisingly, the full-solution processed *is*-OPV with highly competitive mechanical robustness -76.5% of initial PCE after 500 cycles of 10% stretch-release.

Result and discussion

The configuration of the full-solution processed *is*-OPV with the p-i-n structure is shown in Figure 1a. The detailed fabrication procedure is shown in Figure S1 and summarized in the Methods section, SI. The whole device, including the substrate, electrodes, interlayers, and photoactive layers were all fabricated from the solution process (no vacuum-based deposition) (Figure 1b). In this work, AAA composition serves as the electron-transport layer (ETL) and stretchable transparent cathode (*is*-cathode). AgNWs embedded TPU serves as the stretchable substrate and front transparent anode (*is*-anode). PEDOT:PSS (Clevios P VP AI4083, Heraeus) is used as the hole transport layer (HTL). PM6: BTP-eC9, PM6:PY-IT, and PBDB-T: N2200 with different ductility were selected as the active layers. The *is*-OPV is semi-transparent (Figure 1c), twistable, and intrinsically stretchable (Figure 1d). Moreover, the *is*-OPV could conformably attach to the human skin and easily power a sports watch under sunlight exposure which indicates the huge potential in wearable applications (Figure 1e). All the devices were tested with the bottom illumination if not specified.

Is-cathode

The wide-used organic electrolytes ETL (*e. g.* PFN-Br, PDINO) cannot satisfy the requirement of solution-processed AgNWs back cathode because they are ultra-thin and easily dissolved in polar solvents (*e. g.* methanol, IPA), which have been commonly used to disperse AgNWs. In this work, AZO nanoparticles are employed as the ETL above the active layer. The device performances are

insensitive to AZO thickness in the range of 25-80 nm (Figure S2, Table S1, SI). This thickness-insensitivity of AZO would facilitate large-scale production. Meanwhile, the scanning electron microscope (SEM) image (Figure S3a, SI) shows that the AZO ETL still keeps uniform and dense after coating IPA. And the absorption spectra of AZO film are unchanged before and after IPA coating (Figure S3b, SI). It indicates the AZO ETL is sufficiently robust to support the solution-processed back electrode.

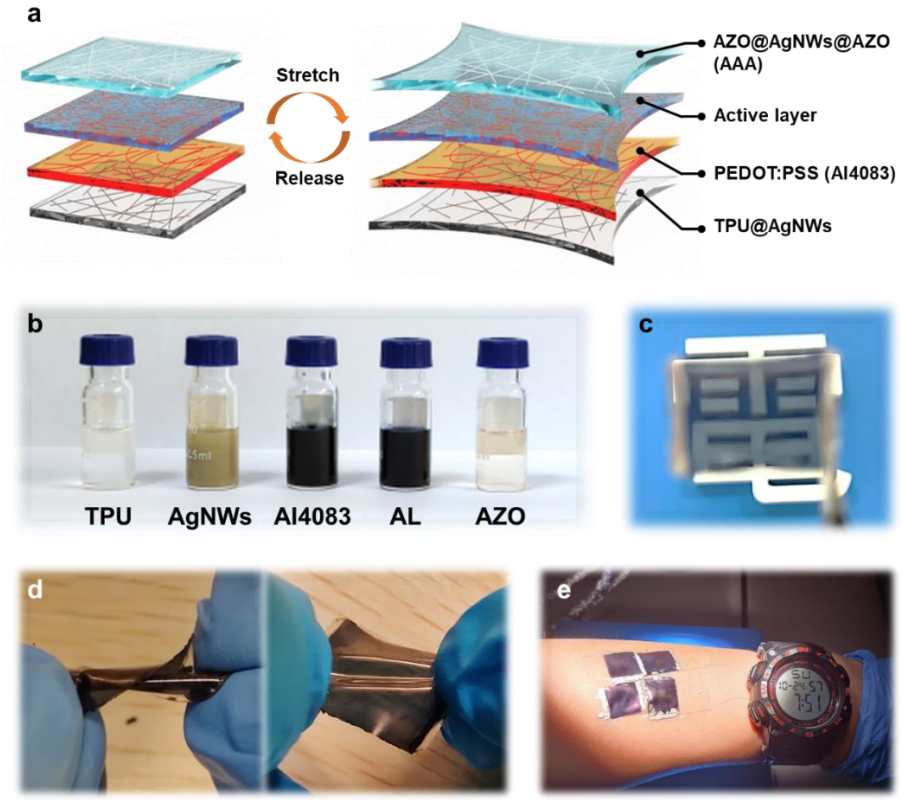

Figure 1 a) Schematic diagram of the is-OPV based on the configuration of TPU@AgNWs/PEDOT:PSS/active layer/AAA; b) Solutions of the materials in each functional layer; c) Photograph of the semi-transparent *is*-OPV; d) Photographs of *is*-OPV for demonstrating twisted and stretchable; e) Four *is*-OPV attach on the skin to power a watch by series connect

AAA composited *is*-cathode is achieved by sequentially coating AgNWs and a second AZO layer onto the existing AZO ETL. The cross-section SEM images of the AAA *is*-cathode on the active layer suggest that the active layer, AZO, and AgNWs are stacked tightly (Figure 2a). It indicates that solution-processed AAA *is*-cathode would form a well-contact configuration and not damage the underlying layers, which is an important requirement of the full solution process. Here, the AZO (ETL)/AgNWs (back electrode) is used as the control group. With the concentration of AgNWs dispersion increased from 3 to 10 mg/ml in IPA, the R_{sh} of the obtained AgNWs networks on AZO decreases significantly from 1863.1 to 16.2 Ω/sq due to the increased density of AgNWs networks (Figure S4a, SI). However, the devices based on AZO/AgNWs as the back interlayer/electrode show poor photovoltaic performance. With AgNWs' concentration increases, the PCE shows increased

tendency but is still not good, especially for the fill factor (FF), which is lower than 60% even with 16.2 Ω/sq AgNWs electrode (Figure S5, Table S2, SI). It indicates that the conductivity of the AgNWs networks (electrode) itself is not the most key factor limiting the performance.

Notably, we found that with the same concentration and spinning speed, the R_{sh} of AgNWs networks spin-coated on the AZO surface is much larger than it is on glass (Figure S4b, SI). Here are two possible reasons: first, due to the different surface potential, the wettability of the AZO surface is not as good as neat glass, which leads to sparser AgNWs networks (Figure S4c, SI). Second, the thermal annealing condition of AgNWs/glass is 150-200℃/20 min, while the AgNWs/AZO is 100℃/10 min considering the existence of the active layer. So, the welding of AgNWs at a high temperature in the back electrode case is not obvious, which has a negative influence on the conductivity (Figure S4d, SI).

In contrast, the devices based on AAA show higher performances. The device was fabricated with the configuration of ITO/PEDOT:PSS/PM6:BTP-eC9/AAA. The energy diagram of the device is provided in Figure S6a while the work function of the AAA is obtained from ultraviolet photoelectron spectroscopy (Figure S6b). The AZO coverage in AAA was first regulated by tuning the AZO concentrations (Figure S7-8 and Table S3, SI). The photovoltaic performance of the AAA-based devices is significantly improved after an AZO coverage with low concentration (0.5% in IPA). Further efficiency improvements are observed with increased AZO concentrations until it reaches 1.67%. The PCE is not affected when the AZO concentration increased to 2.5%. The PCE improvement of AAA-based OPV might be attributed to the optimized charge transport and collections which would be explained later. As a result, the devices based on AAA offer a champion PCE of 12.83% when illuminated from the bottom side, with open-circuit voltage (V_{OC}), short-circuit current density (J_{SC}), and FF of 0.834 V, 20.87 mA·cm^{-2}, and 0.737, respectively (Figure 2b). When illuminated from the AAA side, the device shows relatively lower efficiency (Figure S9, SI). Whereas the control group based on bare AgNWs shows a poor PCE of 7.46% (V_{OC} of 0.811 V, J_{SC} of 18.51 mA·cm^{-2}, and FF of 0.497). Moreover, the AAA shows a low R_{sh} of 30.6 Ω/sq which is much lower than that of bare AgNWs/AZO ETL (without AZO coverage) of 97.4 Ω/sq, which indicates the AZO coverage could effectively improve the conductivity of the AgNWs networks (Figure S10). The increased J_{SC} is proved by the external quantum efficiency (EQE) spectra (Figure 2c). The EQE spectra of the device based on AAA show a similar shape to bare AgNWs, but higher EQE values in the range of 400-850 nm. The current density calculated from EQE is 20.1 and 16.9 mA·cm^{-2}, respectively, which is consistent with J_{SC} from *J-V* curves. The AAA-based semi-transparent device shows comparable photovoltaic performance to the counterpart which is fabricated with an ultra-thin (10-nm) Ag back electrode based on a vacuum thermal evaporation (Figure S11).

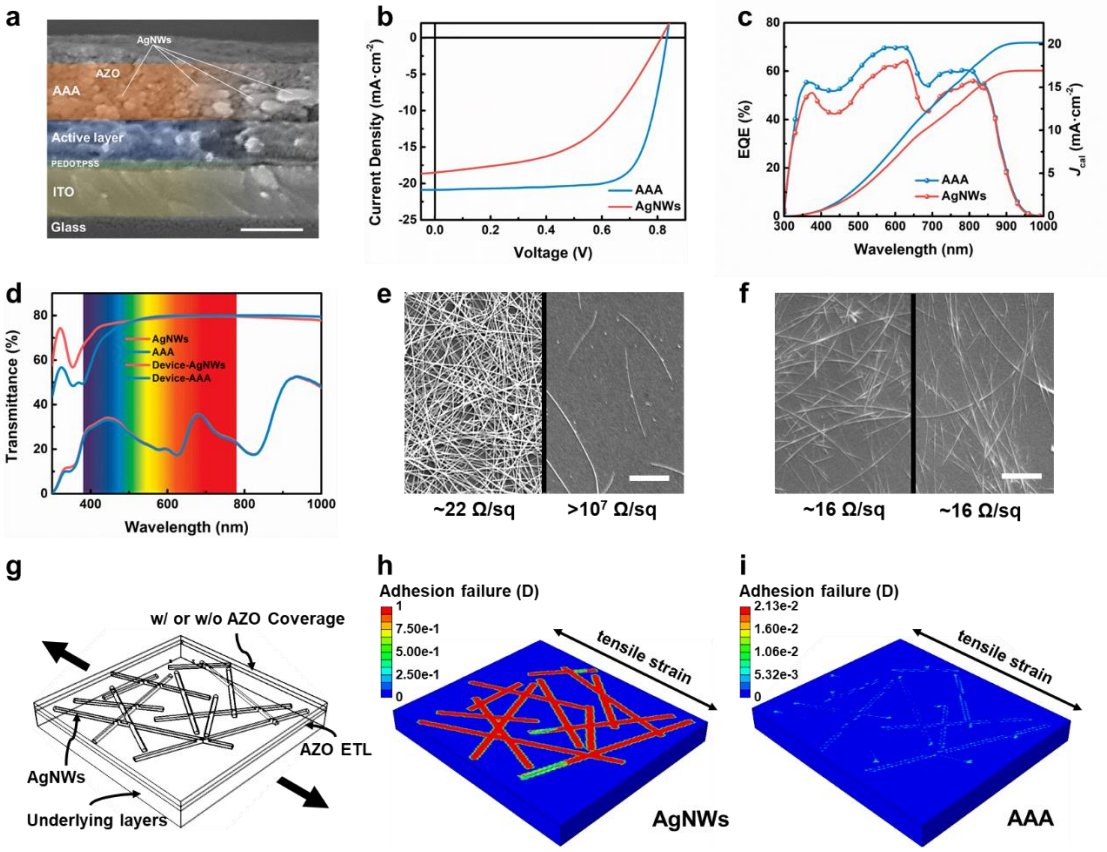

Figure 2 a) Cross-sectional SEM image of the OPV device based on solution-processed AAA back electrode (scale bar: 160 nm); b) *J-V* curves of the semi-transparent devices based on bare AgNWs and AAA as the back electrodes; c) EQE spectra of the semi-transparent devices based on bare AgNWs and AAA as the back electrodes; d) Optical transmittance of the bare AgNWs, AAA back electrodes, and corresponding OPV devices; e) SEM images of the AgNWs/AZO before and after 50 cycles of tape test (scale bar: 2.5 μm); f) SEM images of the AAA before and after 50 cycles of tape test (scale bar: 2.5 μm); g) Schematic diagram of the modeling for mechanical simulations with the device based on the AgNWs and AAA back electrodes; h) Adhesion failure between ETL and AgNWs back electrode under 20% tensile strain; i) Adhesion failure between ETL and AgNWs in AAA back electrode under 20% tensile strain; the AgNWs and AZO coverage are hidden for the visibility of the adhesion failure results.

The optical transmittance of AAA and AZO/AgNWs and corresponding devices were investigated (Figure 2d). The AAA shows decreased transmittance in the range of 300-450 nm, but higher transmittance in the range of 600-1000 nm. The transmittance decrease in the short-wavelength range is attributed to the absorption of extra AZO. While the transmittance enhancement in the long-wavelength range might be attributed to the light-scattering effect of AZO nanoparticles. The overall transmittance between AAA and bare AgNWs is similar. Moreover, the AVT in the range of 380-780 nm is 26.45% of AAA-based devices, which is comparable to AgNWs (26.99%). In this case, the strategy of composited AAA back electrode provides a significant PCE improvement without sacrificing transparency.

The stability of the AAA *is*-cathode was investigated. The conductivity of the AAA *is*-cathode under

mechanical deformation was measured statically and dynamically (Figure S12, SI). The AAA *is*-cathode could maintain good electrical conductivity under 50% strain. After 1000 cycle times of the 20% strain-release process, the AAA *is*-cathode still shows good conductivity.[46] The morphology of the AAA electrode after deformation is investigated by the SEM (Figure S13, SI). Despite nanoscaled cracks observed in inorganic AZO nanoparticles after hundreds of stretch-release cycles, the AgNWs still did not fracture in cracks, answering the high conductivity retention ability of the AAA electrode after deformations. More importantly, the AZO nanoparticles still tightly bundle with AgNWs without falling off, which may not have a major impact on the charge transport and collection ability of the AAA which would be discussed later. Moreover, the tape test was applied to measure the adhesion in the ETL/electrode interface. After 50 cycles of 3M tape adhesion/peel-off, the bare AgNWs network on AZO shows intensive film destruction and loses its conductivity with R_{sh} of over 10^7 Ω/sq (Figure 2e). In contrast, the AAA networks show no obvious morphology destruction, and the R_{sh} remains consistent (Figure 2f). In addition, the air ambient stability (at room temperature and relative humidity of about 40%) of the AAA and bare AgNWs was investigated (Figure S14, SI). The R_{sh} of AgNWs is drastically increased over 12 times within 20 days which might be due to the oxidation of AgNWs when expose to oxygen and water. Nevertheless, the R_{sh} increase of AAA *is*-cathode is less than 2 times over a month, which is a result of the overlaid of extra AZO to form a well-encapsulation.[47-50] In addition, the AAA electrode shows good light stability under 100 mW·cm^{-2} illumination and thermal stability under 80℃ in ambient conditions (Figure S15, SI).

The tape test shows the strong adhesion in AAA under vertical (perpendicular to the device plane) force/strain. However, the adhesion state of the electrodes under "horizontal" (parallel to the device plane) tensile strain is still unclearly. In this case, two simplified finite element models (FEM) were established for simulating the interface adhesion in bare AgNWs/AZO and AAA STE under "horizontal" tensile strains. The process of simulations and the detailed default parameters are provided in the Methods section, SI. In model 1 for bare AgNWs, several nanowires with random postures were placed on the AZO ETL, while in model 2 the nanowires were covered by the extra AZO (Figure 2g). An adhesive contact algorithm was implemented for modeling the interaction between the nanowires and the AZO ETL, which is governed by a bi-linear cohesive zone model (CZM).[51, 52] The adhesion failure degree (D) of the CZM can define the detachment of the nanowires on the AZO ETL. When the tensile strain is applied to the entire model, the D value is gradually increased, which indicates the start of interface detachment (Video S1, SI). When 20% tensile strain is applied, the adhesion failure in bare AgNWs/AZO interface reaches 1 means the complete detachment of the AgNWs on AZO ETL (Figure 2h). Despite the AgNWs networks not being peeled off, it could be regarded as a partial disconnection between AgNWs and AZO ETL, which lead to the "invalid area" of the device. In contrast, the adhesion failure in AgNWs/AZO in AAA composited STE is at least 3-4 orders of magnitude lower than the counterpart in bare AgNWs/AZO (Figure 2i). Benefiting from the reinforced concrete-like 3D-bundling structures, the AAA shows a

strong adhesion than bare AgNWs on AZO ETL under “horizontal” tensile strain, which is critical for stretchable OPV.

To better understand the detailed morphology of the back electrode, the SEM images of the bare AgNWs on AZO, the AAA *is*-cathode, and the AZO ETL were measured from the 45° angle of inclination. As seen in Figure 3a, the AgNWs networks are randomly distributed on the surface of AZO. On the one hand, only physical stacking was observed between the nanowires without welding at the junctions, which would inevitably lead to strong contact resistance between AgNWs.[53] This is one of the reasons for the relatively low conductivity of AgNWs networks on AZO. On the other hand, there is full of void space not only observed within the AgNWs networks but also between AgNWs and AZO ETL (white arrow). The random distribution of nanowire in micro/nano-scale makes a quasi-3D interface between the AgNWs and the AZO ETL. The void space at the AgNWs/AZO interface will always exist, no matter how high the concentration of AgNWs dispersion is used. Such void space at the ETL/electrode interface would make a serious contact issue and reduce the effective area of charge transport and collection.[54] This low-efficient charge transport and collection is responsible for the low FF of AgNWs-based devices. In contrast, in AAA *is*-cathode, the void space within AgNWs networks is mostly filled by the AZO nanoparticle (Figure 3b). More importantly, it seems that the void space (gap) at AgNWs/AZO ETL interface is filled with extra AZO coverage. Compared to the bare AgNWs electrode on AZO ETL, the high-conductive AgNWs are tightly bundled by the surrounding AZO nanoparticles making the AAA more robust. Figure 3c provides the SEM images of the two layers of AZO by sequential deposition without AgNWs. The film shows a smooth morphology which proves the AZO would not be washed away from the further coating.

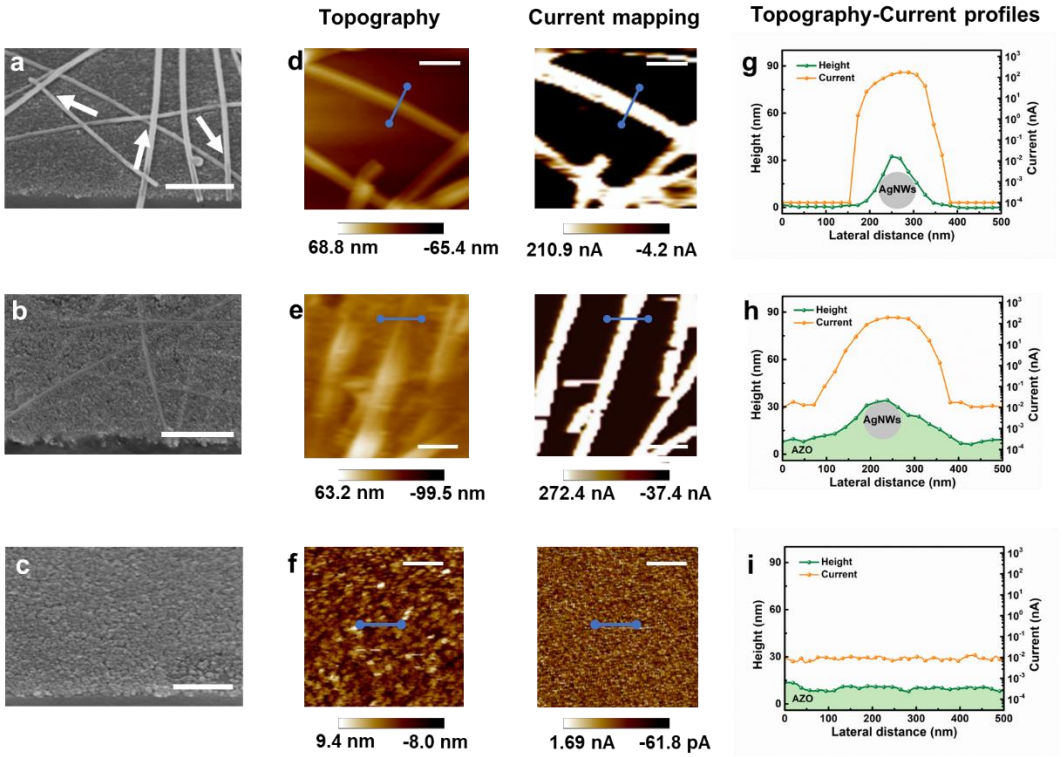

Figure 3 SEM images of a) AZO/AgNWs, b) AAA, and c) AZO films on the glass (scale bar: 500 nm); AFM topographic images and the PeakForce TUNA conductive images of d) bare AgNWs, e) AAA, and f) AZO films on the glass (scale bar: 300 nm); g-i) 1-D line profiles for the topographic and current mapping along the blue line from corresponding images.

To investigate the electrical conducting behaviors in detail, the PeakForce TUNA mode from the atomic force microscope (AFM) was performed. The samples were fabricated by coating bare AgNWs, AAA, and bare AZO on glass. Figure 3d-3f describe the topography and the current mapping of the AgNWs/AZO, AAA, and bare AZO, respectively. An external bias of 0.4 V was applied between the probe and the samples. The 1-D line profiles for the height and current along the blue lines were measured. The diameter of the AgNWs measured from the height difference in topography is approximately 30 nm, which is consistent with the result revealed from SEM. Please note the profile broadening effect of AFM due to the tip-sample convolution makes the measured width of AgNWs larger than height. In the lateral direction, the width of the conductive region is wider than the width of the AgNWs region.[55] The extended conductive region might be ascribed to the low conduction when the probe approaches the AgNWs under the external bias. The high-conductive region (≥10 nA) is approximately 145 nm, which is similar to the lateral width of AgNWs (Figure 3g). Apparently, all the current can only flow through the AgNWs networks, and no lateral current is observed in the void space of AgNWs networks. In contrast, there is the lateral current observed at locations containing no AgNWs in the AAA electrode. The value of lateral current flow through the AAA shows a minimum of 10^{-2} nA, which is the electrical conduction from AZO nanoparticles(Figure 3h-3i). More importantly, the high-conductive region (≥10 nA) in the AAA electrode is approximately 187 nm, and the region for the current in the range of ≥1 nA is

about 232 nm. The extended conductive area indicates good charge transport between AgNWs and AZO as well as an enlarged effective area of charge collection.

Meanwhile, the COMSOL Multiphysics based on the finite element method was employed to simulate the charge carrier collection behavior in bare AgNWs/AZO and AAA STE. The AgNWs were simplified in cross arrangement upon AZO ETL, while the extra AZO with different thickness covers the AgNWs to form the AAA STE (Figure S16-17). The details of the COMSOL simulation are provided in the Methods section, SI. The electric potentials in the interface are mainly distributed along with the AgNWs which are observed in all models. In bare AgNWs/AZO electrodes, there is an extremely low electric potential area under the dangling nanowire junction, which leads to poor charge collection (Figure 4a). With the coverage of the extra AZO with different thicknesses (12-90 nm) onto the AgNWs, the overall intensity of the electric potential continuously increases (Figure 4b-4c). In addition, the 1D profiles of electric potential are measured along two lines drawn in Figure 4a. Along line 1, the electric potential profiles become wider with the increased thickness of AZO coverage (Figure 4d). The high-conductive region (10 μV) is about 116 nm for the bare AgNWs and 266/319 nm for the AAA STE with the AZO coverage thickness of 45/90 nm. The extended high-conductive region from the COMSOL simulation is consistent with the PeakForce TUNA results. As AZO coverage increases from 0 nm to 45 nm, the electric potential intensity shows a significant enhancement along line 2, which is due to the fill of the void space between ETL and the dangling part of AgNWs at junctions (Figure 4e). Moreover, Figure 4f illustrates the integral intensity of electric potential. As the AZO coverage thickness increases, the integral electric potential gradually increases. Specifically, the growth rate of intensity decreases when the AZO coverage becomes thicker. The integral intensity tends to the maximum when the AZO coverage shows a similar thickness to 1-2 layers (*e. g.* 40-80 nm) of the AgNWs networks. Further, increasing the AZO coverage would not affect the charge collections, which is consistent with the experimental results. As a result, the AAA STE exhibits over 3 times higher charge collection efficiency than the bare AgNWs electrode. Despite the huge conductivity difference between AgNWs and AZO nanoparticles, the coverage of AZO could significantly improve the charge collection ability. Overall, the limited physical contact of AgNWs/AZO leads to insufficient charge collection which results in poor photovoltaic performance (Figure 4g). In contrast, the AAA STE shows a reinforced concrete 3D bundling structure that facilitates both the lateral and vertical charge collections (Figure 4h) finally enabling outstanding photovoltaic performance.[56, 57]

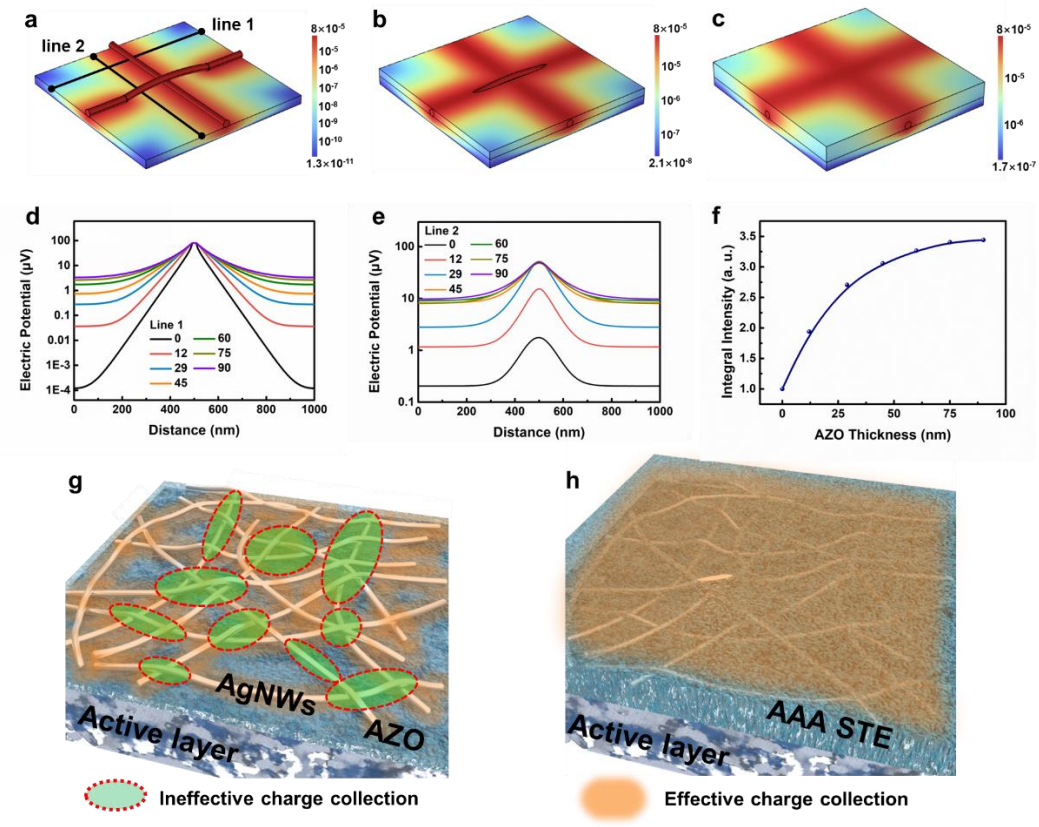

Figure 4 COMSOL electric potential simulation of AAA composited STE with different AZO thickness: a) 0 nm, b) 45, c) 90 nm; One-dimensional line profiles for the electric potential measured along d) line 1, e) line 2 in the AZO (ETL)/ AgNWs interface; f) Normalized integrated intensity of the electric potential mapped in the AZO (ETL)/ AgNWs interface; g-h) Schematic diagram of the bare AgNWs and AAA composited STE with different charge collection capabilities.

To furtherly figure out the relationship between device performance improvement and back electrode optimization, related photophysical measurements were conducted. Series resistance (R_s) and shunt resistance (R_p) of the devices were extracted from the *J-V* curves measured under dark conditions (**Figure S18a**). The R_p is extracted from the reversed saturated current region while the R_s is extracted from the open-circuit region. Benefitting from the reduced area of insufficient charge collection (resistors in parallel), the AAA-based device shows a high R_p of 15455.9 Ωcm^2 which is much higher than the counterpart of AgNWs (2882.5 Ωcm^2). Meanwhile, the decreased R_s of AAA-based devices originate from the enhanced conductivity of the AAA electrode. Moreover, the charge dissociation/collection efficiencies were quantified in **Figure S18b**.[58] The overall charge dissociation/collection probability (*P*) of the devices based on AAA (98.4%) is much higher than AgNWs (84.6%). Since the same active layer with the same charge dissociation probabilities, the improved *P* demonstrates the enhanced charge-collecting ability of the AAA electrode. In addition, the carrier recombination behavior was evaluated by measuring the light-dependent V_{OC} and J_{SC} (**Figure S18c-d**). The ideality factor fitting from light-dependent V_{OC} variation of AgNWs-based device is 1.52 which indicates serious charge recombination happened which is due to the

insufficient charge-collecting ability. The fitted slope value (S) of J_{SC} versus light intensity of AgNWs-based device is only 0.89 which also indicates the nonnegligible bimolecular recombination.[59] In contrast, the ideality factor and S value of AAA-based devices are 1.14 and 0.97 which represent the effectively reduced charge recombination, benefiting from a more sufficient charge collection property of the AAA back electrode.

Is-anode

Thermoplastic elastomer TPU is employed as the substrate due to its high transparency, biocompatibility, solution-processability, and excellent mechanical properties. A low elastic modulus of 20 MPa and high elongation at a break of over 600% makes TPU easily realize conformal contact with expandable skins (Figure 5a). High conductivity, good transparency, and strong adhesion to the substrate are needed by the front electrode of *is*-OPV. AgNWs are promising candidates but show large roughness and poor adhesion when directly coated on the plastic substrate. TPU@AgNWs through the transfer method overcome these disadvantages (Figure 5b). It's seen in SEM images (Figure 5c) that the AgNWs networks are partially embedded into the TPU matrix. This feature is highly desirable for *is*-OPV because it reduces the surface roughness of the AgNWs with a root mean square (RMS) value of 2.97 nm (Figure 5e). Meanwhile, the HTL PEDOT:PSS (AI 4083) can be easily coated onto the TPU@AgNWs with a uniform and smooth surface (Figure 5d). After coating PEDOT:PSS HTL, the RMS of the film is 1.85 nm (Figure 5f). The flat and smooth surface of TPU@AgNWs/PEDOT:PSS would reduce the leakage current originating from the interface and form a high-quality active layer in further steps. The TPU@AgNWs with sheet resistance (R_{sh}) of 24.3 $\Omega\,sq^{-1}$, show an excellent light permeability which presents an average transmittance of 83.2% over the wide range of 300-1000 nm (Figure 5g), which is comparable to the benchmark of the rigid glass/ITO.

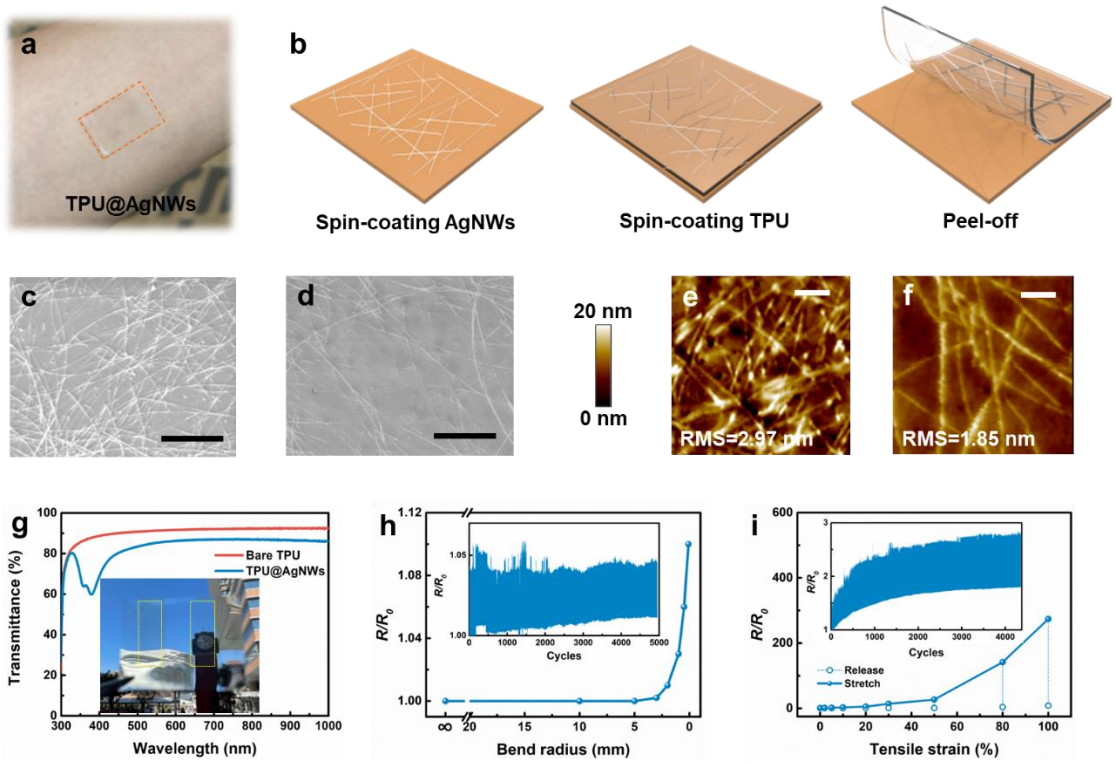

Figure 5 a) Photograph of the TPU@AgNWs STE attach to the skin; b) Schematic diagram of the fabrication of TPU@AgNWs; SEM images of the c) TPU@AgNWs, b) TPU@AgNWs/PEDOT:PSS (AI4083) (scale bar: 5μm); AFM images of the e) TPU@AgNWs, f) TPU@AgNWs/PEDOT:PSS (AI4083) (scale bar: 1μm); g) Transmittance of the bare TPU substrate and TPU@AgNWs STE, inset: photograph of the TPU@AgNWs STE; h) Sheet resistance variation of TPU@AgNWs STE under different bend radius, inset: long-term mechanical stability under continuously bending with a radius of 0.1 mm; i) Sheet resistance variation of TPU@AgNWs STE under different tensile strain, inset: long-term mechanical stability under continuously bending with a tensile strain of 20%.

Different mechanical deformations were applied on TPU@AgNWs *is*-anode to evaluate the mechanical durability. First, no microcracks are observed in our TPU@AgNWs *is*-anode under 100% tensile strain (Figure S19, SI) which is necessary for *is*-OPV. Corresponding conductivity was also real-timely detected. Under bending tests with different radii, the conductivity of TPU@AgNWs *is*-anode barely changed (Figure 5h). The conductivity can also maintain 91% of the initial value even at the extremely small bending radius of 0.1 mm. Moreover, the TPU@AgNWs *is*-anode shows long-term reliability which exhibits within 2% variation about continuously 5000 bending cycles at a bending radius of 2mm (Inset, Figure 5h). More importantly, the TPU@AgNWs *is*-anode shows satisfying durability under different tensile strains (Figure 5i). Specifically, the TPU@AgNWs *is*-anode shows an increased resistance with the enlarged tensile strain and is not failed even at 100% tensile strain. During the long-term stretch-release (20%-0%) process, the TPU@AgNWs *is*-anode also shows impressive reliability (within the 60% conductivity variations) after 4300 cycles of mechanical deformation. In addition, the AgNWs networks embedded into the TPU matrix also provide strong adhesion between AgNWs and TPU (Figure S20, SI). After 50 tape tests, the conductivity of AgNWs@TPU shows no obvious degradation, with the R_{sh} variation being within

10%. As an ideally stretchable interconnector, the TPU@AgNWs *is*-anode easily enables the LED lights on. With the applied tensile strain increased, the LED still works until at a tensile strain of 50%, which proves the practicality of our *is*-anode (Figure S21, SI).

Is-OPV

Based on the transparent *is*-cathode and *is*-anode, the *is*-OPV was fabricated with the configurations of TPU@AgNWs/AI4083/active layer/AAA. The active layer consists of state-of-the-art polymer donor PM6 and small molecule acceptor BTP-eC9 (Figure 6a). The photovoltaic performance of the *is*-OPV is shown in Figure 6b. The *is*-OPV device based on PM6: BTP-eC9 active layer shows a champion PCE of 10.90% with a V_{OC} = 0.812 V, a J_{SC} = 20.31 mA·cm^{-2}, and a FF = 66.1%. Both the rigid device and the *is*-OPV in this work represent the highest performances (especially high FF) of AgNWs-based back electrodes so far (Figure 6c, Appendix S1, SI).

Benefiting from the high optical transmittance of both front STE (TPU@AgNWs) and back STE (AAA), the *is*-OPV shows high transparency with an AVT of 26.64% (Figure 6d). Notably, the photovoltaic performance of *is*-OPV based on the full solution process is not lagged behind the corresponding rigid device based on ITO/glass and ultra-thin Ag as the front and back electrodes. It indicates the great potential of our *is*-OPV structure, especially the design of the *is*-cathode and *is*-anode. And the shelf lifetime of the device is evaluated by storing the unencapsulated device in the dark in an N_2-filled glove box to verify the feasibility of our *is*-OPV. The *is*-OPV shows a PCE retention of 87.3% after 20 days (Figure S22, SI).

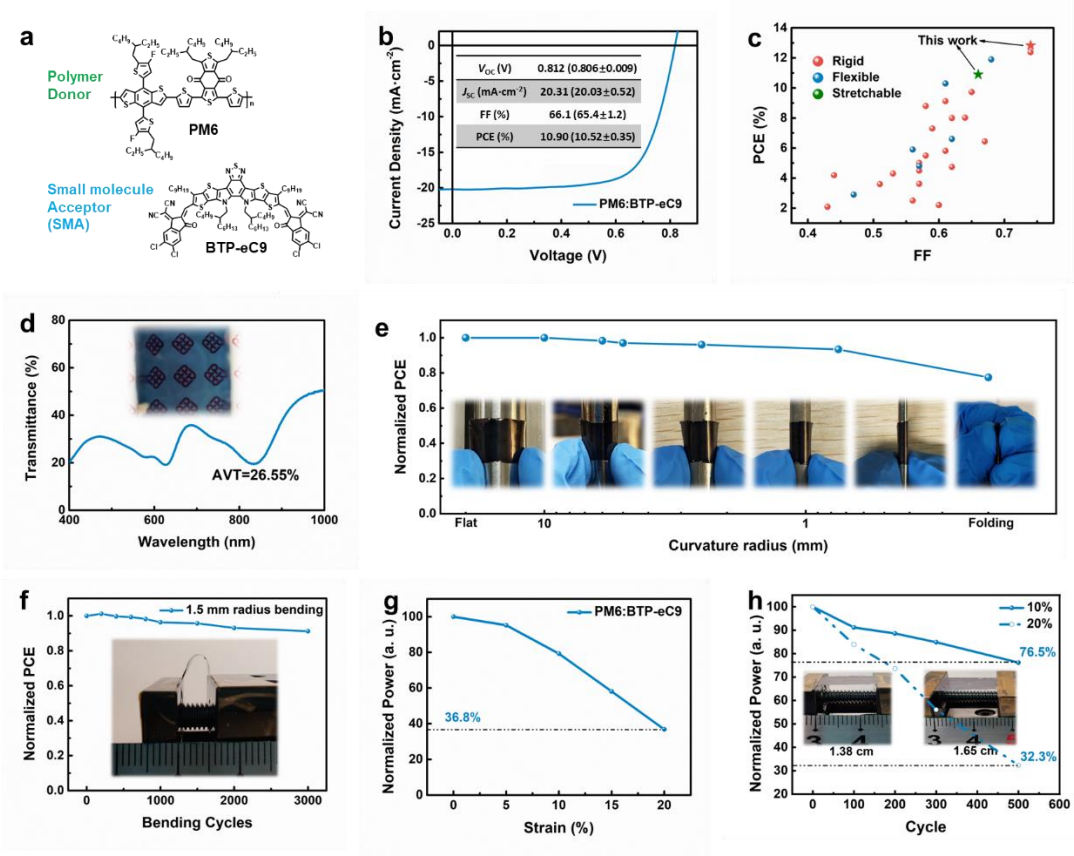

Figure 6 a) Chemical structures of the polymer donor (PM6) and small-molecule acceptor (BTP-eC9); b) *J-V* curve and corresponding parameters of the *is*-OPV based on PM6:BTP-eC9. The average values and the standard deviation were obtained from ten independent cells.; c) PCE and FF comparison of our results and previously reported results in the literature of semi-transparent OPV with the solution-processed back electrode; d) Optical transmittance of the semi-transparent *is*-OPV based on PM6:BTP-eC9; e) Normalized PCE retention of the *is*-OPV after 300 bending cycles with different curvature radius; f) Normalized PCE retention of the *is*-OPV after long-term bending cycles with a radius of 1.5 nm; g) Normalized output power of the *is*-OPV under different tensile strain; h) Normalized output power of the *is*-OPV after 500 stretch-release cycles with 10% and 20% tensile strain

To demonstrate the applicability of *is*-OPV under mechanical deformation, the performance of the *is*-OPV was first measured after the bending test with different bending radii. The bending direction of the device is shown in Figure S23 in SI. Figure 6e exhibits the PCE retention of the *is*-OPV based on 200 cycles of continuous bending with different curvature radii (from flat to 0.75 mm). There is no obvious PCE decay after bending with a curvature radius of 10, 5, and 3 mm. And 93% of initial PCE remains after bending with a curvature radius of 0.75 mm. The device even keeps 76.6% of the initial PCE after 300 cycles of folding. Benefiting from the well-established flexibility of the front and back STE as well as the active layer, the *is*-OPV shows excellent durability under extreme bending and even folding. Moreover, the long-term cyclic bending test was applied to the *is*-OPV (Figure 6f). After 3000 cyclic bending-flatting processes with a 1.5 mm curvature radius, the *is*-OPV exhibits 91.2% PCE retention. The representative *J-V* curves and their detailed parameters are

provided in Figure S24 and Table S5-6, SI. Notably, due to the low elastic modulus of the TPU substrate, the *is*-OPV shows no obvious crease after extreme bending or folding, which is more suitable for wearable applications than other plastic substrates (*i. e.* PET).

The stretchability of the *is*-OPV is in-situ tracked under different tensile strains. Since the effective area of the *is*-OPV is inconsistent during stretching, herein we employed the overall generated power (= PCE×area) as the criteria to evaluate the photovoltaic performance. The *is*-OPV based on PM6: BTP-eC9 exhibits 89.3% of initial output power under 10% strain and 36.8% retention under 20% strain with perpendicular direction (Figure 6g and Figure S25a). Moreover, the output power of the *is*-OPV is tracked after a series of stretch-release cycles (Figure 6h). The *is*-OPV based on PM6: BTP-eC9 exhibits 76.5% of its initial power after 500 cycles of 10% stretch-release process. When the tensile strain is added to 20%, the performance of *is*-OPV based on this system shows relatively poor durability, with only 32.3% PCE retention after 500 cycles of stretch-release processes. The representative *J-V* curves and their detailed parameters are provided in Figure S26 and Table S7-9, SI. The devices show similar efficiency decay when applied with tensile strain with parallel direction (Figure S25b, SI). Since both the front STE (TPU@AgNWs) and back STE (AAA) have proven their stretchability aforementioned, the abrupt PCE degradation may originate from the active layers with limited ductility.

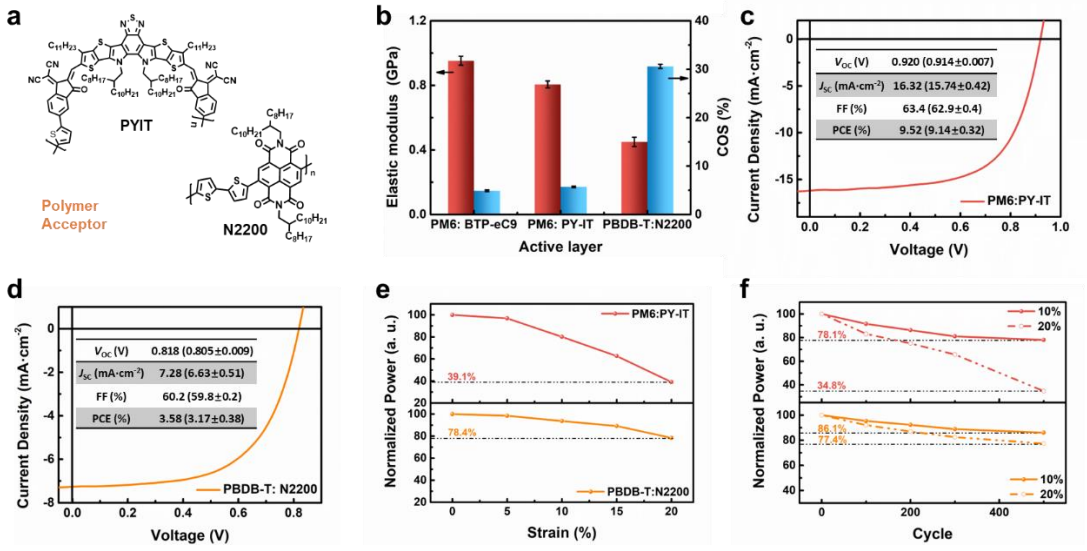

Figure 7 a) Chemical structures of the polymer acceptors PY-IT and N2200; b) Summarized elastic modulus and crack-onset-strain of blend films of active layer systems; *J-V* curve and corresponding parameters of the *is*-OPV based on c) PM6:PY-IT and d) PBDB-T:N2200. The average values and the standard deviation were obtained from ten independent cells.; e) Normalized output power of the *is*-OPV under different tensile strain based on all-polymer systems; f) Normalized output power of the *is*-OPV after 500 stretch-release cycles with 10% and 20% tensile strain.

All-polymer systems have been considered as the active layer candidates to improve the stretchability of *is*-OPV due to their higher ductility than polymer: SMA system. PY-IT is one of the

highest-performed polymer acceptors derived from the Y-series SMA.[60] N2200 is one of the mature polymer acceptors which has been extensively studied (Figure 7a). The mechanical property of these active layer materials has been investigated and summarized (Figure 7b). The elastic modulus of the blend films of the active layers is measured and calculated by the buckling method (Figure S27, SI). The calculated E_f of PM6: BTP-eC9, PM6: PY-IT, and PBDB-T: N2200 are 0.953, 0.806, and 0.550 GPa, respectively. In addition, the crack-onset strains (COS) of these three films are determined by the film-on-elastomer (FOE) method.[61] The formation of the crack was real-time monitored by an optical microscope (Figure S28, SI). The micro-scale cracks appear in the blend films of PM6: BTP-eC9, PM6: PY-IT, and PBDB-T: N2200 when the strains of 4.9%, 5.7%, and 30.6% are applied, respectively. The PM6: BTP-eC9 system shows the highest elastic modulus and the lowest COS values due to the poor ductility of the small molecule acceptor. In contrast, the PBDB-T: N2200 blend film shows the lowest E_f among these three systems which is attributed to the low stiffness of polymer acceptor N2200 based on naphthalene diimide. Notably, the E_f and COS values of all-polymer system PM6: PY-IT are close to the PM6: BTP-eC9 blend film. The state-of-the-art polymer acceptors including PY-IT derived from Y-series small molecules contain largely conjugated backbones, which makes the polymer acceptor as stiff as the small molecules.[62] The highly stiff backbones impede the polymer acceptor with high ductility, despite the outstanding photovoltaic performance.

The photovoltaic and mechanical performance of the *is*-OPV based on all-polymer systems PM6: PY-IT and PBDB-T: N2200 were also investigated. Compared to polymer/SMA systems, the all-polymer systems have relatively lower PCE, which is 9.52% and 3.58% for PM6: PY-IT and PBDB-T: N2200 systems, respectively (Figure 7c-7d). The all-polymer systems show lower PCE than polymer:SMA systems. When replacing the small molecule acceptor BTP-eC9 with its derivative polymer PY-IT, the corresponding *is*-OPV shows a similar deformation resistance, which keeps 80.3% and 39.1% output power retentions under 10% and 20% strains, respectively. The counterpart of another all-polymer system PBDB-T: N2200 are 93.7% and 78.4%. For the long-term cyclic stretch-release process, the *is*-OPV based on PM6: PY-IT presents power retentions of 78.1% and 34.8% after 500 cycles stretch with 10% and 20% strain (Figure 7e). In contrast, benefiting from the high ductility, the *is*-OPV based on PBDB-T: N2200 system can still maintain 86.1% and 77.4% of the initial PCE after 500 cycles stretch with 10% and 20% strain, respectively (Figure 7f). All the representative *J-V* curves and their detailed parameters are provided in Figure S29-30 and Table S7-9, SI. Despite the relatively low initial PCE of PBDB-T: N2200-based *is*-OPV, the excellent durability under tensile strain indicates the huge potential of the *is*-OPV in wearable applications. Apparently, an important factor that influences the power of *is*-OPV under strain is the ductility of the blend films of the active layer. Currently, several methods have been used to improve the ductility of the active layers but affect the photovoltaic performance, inevitably.[29, 63-67] Further exploration like introducing soft linkage in the main chain of polymer acceptors to obtain high-performed polymer acceptors with high ductility is necessary (> 30%).[68]

To prove the versatility of our *is*-anode and *is*-cathode in semi-conductor applications, the organic light-emitting diode (OLED) based on TPU@AgNWs and AAA as the front and back STE was also fabricated. The fabrication details are provided in the Methods section, SI. The detailed parameters including current density-voltage (*J*-*V*), luminance-voltage curves (*L*-*V*), current efficiency (CE) and quantum efficiency (QE), and emission spectra of the *is*-OLED devices are provided in Figure S31 in SI. The turn-on voltage of the *is*-OLED is about 6.6 V. And the *is*-OLED shows a luminance of over 700 $cd \cdot m^{-2}$ under an external voltage of 11 V. Moreover, the highest CE of 1.8 $cd \cdot A^{-1}$ and QE of 0.31% are achieved. The *is*-OLED shows a green emission with a wavelength peak of 534 nm. As seen in Figure S32, the OLED device shows uniform emission at an external bias of 9V under tensile strain by a probe poking.

Conclusion

In summary, we provided a framework for designing intrinsically stretchable, semi-transparent OPVs based on a full solution process. We first designed a ferroconcrete structured AAA back STE which not only offers a 3D long-range pathway for efficient charge transport and collection but also shows a reinforced ETL/STE interface under deformation. The AAA-based OPV shows comparable PCE (12.83%) and AVT (26.7%) to the thermal evaporated ultra-thin Ag electrode. Furtherly, by employing the TPU@AgNWs as the front STE, the semi-transparent *is*-OPV performed a record PCE of 10.90% for the PM6:BTP-eC9 active layer system. For PBDB-T: N2200 all-polymer system, the *is*-OPV maintains 86.1% and 77.4% of the initial PCE after 500 cycles stretch with 10% and 20% strain, respectively. Our work provided an exciting template for fabricating stretchable photovoltaics for wearable/e-skin applications in the future.

Data availability

The authors declare that the experimental data that support the findings of this paper are available within the article and its Supplementary Information files. Other findings in this study are available from the corresponding authors upon reasonable request.

Reference

1. Z. Wen, M. H. Yeh, H. Guo, J. Wang, Y. Zi, W. Xu, J. Deng, L. Zhu, X. Wang, C. Hu, L. Zhu, X. Sun and Z. L. Wang, *Sci. Adv.*, 2016, **2**, 1600097.
2. S. Park, S. W. Heo, W. Lee, D. Inoue, Z. Jiang, K. Yu, H. Jinno, D. Hashizume, M. Sekino, T. Yokota, K. Fukuda, K. Tajima and T. Someya, *Nature*, 2018, **561**, 516-521.
3. H. Jinno, K. Fukuda, X. Xu, S. Park, Y. Suzuki, M. Koizumi, T. Yokota, I. Osaka, K. Takimiya and T. Someya, *Nat. Energy*, 2017, **2**, 780.
4. C. Wang, X. Li, H. Hu, L. Zhang, Z. Huang, M. Lin, Z. Zhang, Z. Yin, B. Huang, H. Gong, S. Bhaskaran, Y. Gu, M. Makihata, Y. Guo, Y. Lei, Y. Chen, C. Wang, Y. Li, T. Zhang, Z. Chen, A. P. Pisano, L. Zhang, Q. Zhou and S. Xu, *Nat. Biomed. Eng.*, 2018, **2**, 687-695.
5. Z. Zhang, W. Wang, Y. Jiang, Y. X. Wang, Y. Wu, J. C. Lai, S. Niu, C. Xu, C. C. Shih, C. Wang, H. Yan,

L. Galuska, N. Prine, H. C. Wu, D. Zhong, G. Chen, N. Matsuhisa, Y. Zheng, Z. Yu, Y. Wang, R. Dauskardt, X. Gu, J. B. Tok and Z. Bao, *Nature*, 2022, **603**, 624-630.

6. N. Matsuhisa, X. Chen, Z. Bao and T. Someya, *Chem. Soc. Rev.*, 2019, **48**, 2946.
7. N. Matsuhisa, S. Niu, S. J. K. O'Neill, J. Kang, Y. Ochiai, T. Katsumata, H. C. Wu, M. Ashizawa, G. N. Wang, D. Zhong, X. Wang, X. Gong, R. Ning, H. Gong, I. You, Y. Zheng, Z. Zhang, J. B. Tok, X. Chen and Z. Bao, *Nature*, 2021, **600**, 246-252.
8. J. Liu, J. Wang, Z. Zhang, F. Molina-Lopez, G. N. Wang, B. C. Schroeder, X. Yan, Y. Zeng, O. Zhao, H. Tran, T. Lei, Y. Lu, Y. X. Wang, J. B. Tok, R. Dauskardt, J. W. Chung, Y. Yun and Z. Bao, *Nat. Commun.*, 2020, **11**, 3362.
9. G. S. Jeong, D. H. Baek, H. C. Jung, J. H. Song, J. H. Moon, S. W. Hong, I. Y. Kim and S. H. Lee, *Nat. Commun.*, 2012, **3**, 977.
10. J. Yuan, Y. Zhang, L. Zhou, G. Zhang, H.-L. Yip, T.-K. Lau, X. Lu, C. Zhu, H. Peng, P. A. Johnson, M. Leclerc, Y. Cao, J. Ulanski, Y. Li and Y. Zou, *Joule*, 2019, **3**, 1140-1151.
11. P. Cheng, G. Li, X. Zhan and Y. Yang, *Nat. Photonics*, 2018, **12**, 131-142.
12. G. Li, C. W. Chu, V. Shrotriya, J. Huang and Y. Yang, *Applied Physics Letters*, 2006, **88**.
13. G. Li, W.-H. Chang and Y. Yang, *Nature Reviews Materials*, 2017, **2**, 17043.
14. L. Zhu, M. Zhang, J. Xu, C. Li, J. Yan, G. Zhou, W. Zhong, T. Hao, J. Song, X. Xue, Z. Zhou, R. Zeng, H. Zhu, C. C. Chen, R. C. I. MacKenzie, Y. Zou, J. Nelson, Y. Zhang, Y. Sun and F. Liu, *Nat. Mater.*, 2022, **21**, 656-663.
15. L. Zhan, S. Li, Y. Li, R. Sun, J. Min, Z. Bi, W. Ma, Z. Chen, G. Zhou, H. Zhu, M. Shi, L. Zuo and H. Chen, *Joule*, 2022, **6**, 662-675.
16. Z. Zheng, J. Wang, P. Bi, J. Ren, Y. Wang, Y. Yang, X. Liu, S. Zhang and J. Hou, *Joule*, 2022, **6**, 171-184.
17. W. Gao, F. Qi, Z. Peng, F. R. Lin, K. Jiang, C. Zhong, W. Kaminsky, Z. Guan, C. S. Lee, T. J. Marks, H. Ade and A. K. Y. Jen, *Adv. Mater.*, 2022, DOI: 10.1002/adma.202202089, 2202089.
18. R. Ma, C. Yan, P. W.-K. Fong, J. Yu, H. Liu, J. Yin, J. Huang, X. Lu, H. Yan and G. Li, *Energy Environ. Sci.*, 2022, **15**, 2479-2488.
19. J. Qin, L. Lan, S. Chen, F. Huang, H. Shi, W. Chen, H. Xia, K. Sun and C. Yang, *Adv. Funct. Mater.*, 2020, **30**, 2002529.
20. D. J. Lipomi, B. C. Tee, M. Vosgueritchian and Z. Bao, *Adv. Mater.*, 2011, **23**, 1771-1775.
21. W. Huang, Z. Jiang, K. Fukuda, X. Jiao, C. R. McNeill, T. Yokota and T. Someya, *Joule*, 2020, **4**, 128-141.
22. M. Kaltenbrunner, M. S. White, E. D. Glowacki, T. Sekitani, T. Someya, N. S. Sariciftci and S. Bauer, *Nat. Commun.*, 2012, **3**, 770.
23. Z. Jiang, F. Wang, K. Fukuda, A. Karki, W. Huang, K. Yu, T. Yokota, K. Tajima, T. Q. Nguyen and T. Someya, *Proc. Natl. Acad. Sci. U.S.A.*, 2020, **117**, 6391-6397.
24. J. Willmann, D. Stocker and E. Dörsam, *Organic Electronics*, 2014, **15**, 1631-1640.
25. Z. Wang, M. Xu, Z. Li, Y. Gao, L. Yang, D. Zhang and M. Shao, *Adv. Funct. Mater.*, 2021, **31**,

2103534.

26. Q. Zhu, J. Xue, L. Zhang, J. Wen, B. Lin, H. B. Naveed, Z. Bi, J. Xin, H. Zhao, C. Zhao, K. Zhou, S. Frank Liu and W. Ma, *Small*, 2021, **17**, 2007011.
27. J. Wang, K. Fukuda, D. Inoue, D. Hashizume, L. Sun, S. Xiong, T. Yokota and T. Someya, *ACS Appl. Mater. Interfaces*, 2022, **14**, 14165-14173.
28. J. Noh, G.-U. Kim, S. Han, S. J. Oh, Y. Jeon, D. Jeong, S. W. Kim, T.-S. Kim, B. J. Kim and J.-Y. Lee, *ACS Energy Lett.*, 2021, **6**, 2512-2518.
29. J. W. Lee, G. U. Kim, D. J. Kim, Y. Jeon, S. Li, T. S. Kim, J. Y. Lee and B. J. Kim, *Adv. Energy Mater.*, 2022, DOI: 10.1002/aenm.202200887, 2200887.
30. M. R. Azani, A. Hassanpour and T. Torres, *Adv. Energy Mater.*, 2020, **10**, 2002536.
31. Y. Yang, B. Xu and J. Hou, *Chin. J. Chem.*, 2021, **39**, 2315-2329.
32. J. H. Seo, I. Hwang, H. D. Um, S. Lee, K. Lee, J. Park, H. Shin, T. H. Kwon, S. J. Kang and K. Seo, *Adv. Mater.*, 2017, **29**, 1701479.
33. X. Chen, G. Xu, G. Zeng, H. Gu, H. Chen, H. Xu, H. Yao, Y. Li, J. Hou and Y. Li, *Adv. Mater.*, 2020, **32**, 1908478.
34. N. Cui, Y. Song, C.-H. Tan, K. Zhang, X. Yang, S. Dong, B. Xie and F. Huang, *npj Flex. Electron.*, 2021, **5**.
35. G. Zeng, W. Chen, X. Chen, Y. Hu, Y. Chen, B. Zhang, H. Chen, W. Sun, Y. Shen, Y. Li, F. Yan and Y. Li, *J. Am. Chem. Soc.*, 2022, **144**, 8658-8668.
36. S. Ye, A. R. Rathmell, Z. Chen, I. E. Stewart and B. J. Wiley, *Adv. Mater.*, 2014, **26**, 6670-6687.
37. C. Ma, Y. F. Liu, Y. G. Bi, X. L. Zhang, D. Yin, J. Feng and H. B. Sun, *Nanoscale*, 2021, **13**, 12423-12437.
38. D. Wang, Y. Zhang, X. Lu, Z. Ma, C. Xie and Z. Zheng, *Chem. Soc. Rev.*, 2018, **47**, 4611-4641.
39. D. Langley, G. Giusti, C. Mayousse, C. Celle, D. Bellet and J. P. Simonato, *Nanotechnology*, 2013, **24**, 452001.
40. J. Chae, H. Kim, S.-M. Youn, C. Jeong, E.-M. Han, C. Yun and M. H. Kang, *Org. Electron.*, 2021, **89**, 106046.
41. J. Y. Lee, S. T. Connor, Y. Cui and P. Peumans, *Nano Lett.*, 2010, **10**, 1276-1279.
42. M. H. Kang, H. Kim and C. Yun, *Energy Sci. Eng.*, 2022, **10**, 1153-1163.
43. Y. Xiong, R. E. Booth, T. Kim, L. Ye, Y. Liu, Q. Dong, M. Zhang, F. So, Y. Zhu, A. Amassian, B. T. O'Connor and H. Ade, *Solar RRL*, 2020, **4**, 2000328.
44. H. I. Jeong, S. Biswas, S. C. Yoon, S. J. Ko, H. Kim and H. Choi, *Adv. Energy Mater.*, 2021, **11**, 2102397.
45. J.-J. Shen, *Synth. Met.*, 2021, **271**, 116582.
46. W.-C. Tsai, S. R. Thomas, C.-H. Hsu, Y.-C. Huang, J.-Y. Tseng, T.-T. Wu, C.-h. Chang, Z. M. Wang, J.-M. Shieh, C.-H. Shen and Y.-L. Chueh, *J. Mater. Chem. A*, 2016, **4**, 6980-6988.
47. J. J. Patil, W. H. Chae, A. Trebach, K. J. Carter, E. Lee, T. Sannicolo and J. C. Grossman, *Adv. Mater.*, 2021, **33**, 2004356.

48. T. Sannicolo, W. H. Chae, J. Mwaura, V. Bulović and J. C. Grossman, *ACS Appl. Energy Mater.*, 2021, **4**, 1431-1441.
49. X. Zhang, J. Wu, J. Wang, Q. Yang, B. Zhang and Z. Xie, *ACS Appl. Mater. Interfaces*, 2016, **8**, 34630-34637.
50. Q. Huang, W. Shen, X. Fang, G. Chen, Y. Yang, J. Huang, R. Tan and W. Song, *ACS Appl. Mater. Interfaces*, 2015, **7**, 4299-4305.
51. N. Lu, Z. Suo and J. J. Vlassak, *Acta Mater.*, 2010, **58**, 1679-1687.
52. H. Hu, H. Tian, Y. Gao, Z. Wan, L. Wang, H. Xu, C. Wang, J. Shao and Z. Zheng, *Journal of the Mechanics and Physics of Solids*, 2023, **170**, 105121.
53. M. Zhang, S. Han, Z. Y. Xuan, X. Fang, X. Liu, W. Zhang and H. J. Chen, *Micromachines*, 2021, **12**, 618.
54. L. Sun, W. Zeng, C. Xie, L. Hu, X. Dong, F. Qin, W. Wang, T. Liu, X. Jiang, Y. Jiang and Y. Zhou, *Adv. Mater.*, 2020, **32**, 1907840.
55. A. Kim, Y. Won, K. Woo, S. Jeong and J. Moon, *Adv. Funct. Mater.*, 2014, **24**, 2462-2471.
56. C. H. Chung, T. B. Song, B. Bob, R. Zhu, H. S. Duan and Y. Yang, *Adv. Mater.*, 2012, **24**, 5499-5504.
57. C.-H. Chung, T.-B. Song, B. Bob, R. Zhu and Y. Yang, *Nano Res.*, 2012, **5**, 805-814.
58. X. Chen, G. Xu, G. Zeng, H. Gu, H. Chen, H. Xu, H. Yao, Y. Li, J. Hou and Y. Li, *Advanced Materials*, 2020, **32**, 1908478.
59. X. Li, R. Xia, K. Yan, J. Ren, H.-L. Yip, C.-Z. Li and H. Chen, *ACS Energy Letters*, 2020, **5**, 3115-3123.
60. Z. Luo, T. Liu, R. Ma, Y. Xiao, L. Zhan, G. Zhang, H. Sun, F. Ni, G. Chai, J. Wang, C. Zhong, Y. Zou, X. Guo, X. Lu, H. Chen, H. Yan and C. Yang, *Advanced Materials*, 2020, **32**, 2005942.
61. J. S. Park, G. U. Kim, S. Lee, J. W. Lee, S. Li, J. Y. Lee and B. J. Kim, *Adv. Mater.*, 2022, DOI: 10.1002/adma.202201623, 2201623.
62. R. J. Ma, K. K. Zhou, Y. N. Sun, T. Liu, Y. Y. Kan, Y. Q. Xiao, T. A. Dela Pena, Y. X. Li, X. H. Zou, Z. S. Xing, Z. H. Luo, K. S. Wong, X. H. Lu, L. Ye, H. Yan and K. Gao, *Matter*, 2022, **5**, 725-734.
63. Z. Wang, D. Zhang, M. Xu, J. Liu, J. He, L. Yang, Z. Li, Y. Gao and M. Shao, *Small*, 2022, **18**, 2201589.
64. Z. Peng, K. Xian, Y. Cui, Q. Qi, J. Liu, Y. Xu, Y. Chai, C. Yang, J. Hou, Y. Geng and L. Ye, *Adv Mater*, 2021, **33**, 2106732.
65. C. Yan, J. Qin, Y. Wang, G. Li and P. Cheng, *Adv. Energy Mater.*, 2022, DOI: 10.1002/aenm.202201087, 2201087.
66. J. Han, F. Bao, X. Wang, D. Huang, R. Yang, C. Yang, X. Jian, J. Wang, X. Bao and J. Chu, *Cell Rep. Phys. Sci.*, 2021, **2**, 100408.
67. C. Xie, C. Xiao, X. Jiang, S. Liang, C. Liu, Z. Zhang, Q. Chen and W. Li, *Macromolecules*, 2021, **55**, 322-330.
68. J.-W. Lee, D. Jeong, D. J. Kim, T. N.-L. Phan, J. S. Park, T.-S. Kim and B. J. Kim, *Energy Environ. Sci.*, 2021, **14**, 4067.

Acknowledgements

The authors acknowledge the support by the Research Grants Council of Hong Kong (Project Nos Project Nos 15320216, 15221320, C5037-18G), RGC Senior Research Fellowship Scheme (SRFS2122-5S04), National Natural Science Foundation of China (51961165102), Shenzhen Science and Technology Innovation Commission (JCYJ20200109105003940, SGDX2019081623220944), the Hong Kong Polytechnic University Internal Research Funds: Sir Sze-yuen Chung Endowed Professorship Fund (8-8480), RISE (1-CDA5), 1-W15V, and Guangdong-Hong Kong-Macao Joint Laboratory for Photonic-Thermal-Electrical Energy Materials and Devices (GDSTC No. 2019B121205001).

Author contributions

J.Huang and Z.L. contributed equally to this work. G.L. and J.Huang conceived the idea. G.L. supervised the work. J.Huang, Z.L., and G.L. designed the experiments. J.Huang and Z.L. carried out the device fabrication and majority device characterization. J.He and H.Y. carried out the electrical simulation. H.H. and Z.Z. carried out the mechanical simulation. Q.L. carried out the SEM test. K.L. and Y.Z. carried out the AFM test. Z.R. graphed and analyzed the data. J.Huang and G.L. wrote and revised the manuscript. All authors discussed the results and commented on the manuscript.

Competing interests

The authors declare that they have no competing interests.